Check for updates

Small

NANO · MICRO small
www.small-journal.com

RESEARCH ARTICLE

Hierarchical Porous Carbons for High-Rate Aqueous Supercapacitors: Tuning Pore Sizes by Molecular Design of Carbon Dots as Self-Templates

Xi-Rong Zhang | Hao-Wen Sun | Ling Xiao | Yong-Gang Wang | Huan-Ming Xiong

Department of Chemistry, Shanghai Key Laboratory of Electrochemical and Thermochemical Conversion for Resources Recycling, Fudan University, Shanghai, P. R. China

Correspondence: Yong-Gang Wang (ygwang@fudan.edu.cn) | Huan-Ming Xiong (hmxiong@fudan.edu.cn)

Received: 31 July 2026 | **Revised:** 27 September 2026 | **Accepted:** 9 October 2026

Keywords: carbon dot | porous carbon | self-template | supercapacitor

ABSTRACT

Rational pore-size regulation is central to high-performance electric double-layer capacitors, yet carbon dots (CDs) self-templating often yields overly micropore-dominated carbons with limited high-rate capability. Here, we tailor CDs by combining polyethyleneimine with four organic acids and convert them into porous carbons, eliminating high-temperature corrosive chemical activation. Systematic porosimetry reveals a direct link between CDs molecular architecture and the resulting pore-size distributions. Notably, a mesopore-enriching pathway is identified, allowing hierarchical micro/mesoporosity. The optimized sample (PC-PMDA) delivers 582 F g^{-1} at 1 A g^{-1} and retains 475 F g^{-1} at 60 A g^{-1} with an IR drop of 0.09 V. At a practical mass loading of 10 mg cm^{-2}, 78% of the capacity (relative to that at low loading) is still retained. This study provided a mechanistic picture of pore generation by CDs self-templating.

1 | Introduction

Porous carbon materials have attracted extensive attention owing to their high specific surface area (SSA), tunable pore architecture, good electrical conductivity, and excellent chemical stability, which make them promising candidates for applications in adsorption, catalysis, and electrochemical energy storage [1–6]. Among these applications, porous carbons are the most widely used electrode materials for supercapacitors, particularly the electric double-layer capacitor (EDLC), due to their low cost, abundant resources, and structural design flexibility [7, 8]. By far, the rational regulation of pore size distributions has been widely recognized as a critical factor governing the electrochemical performance of porous carbon electrodes [8–10]. On one hand, micropores (< 2 nm) are dominant in enlarging the SSA and increasing charge storage sites, thereby contributing to high specific capacitance directly [11–13]. On the other, mesopores (2–50 nm) serve as efficient ion transport pathways and electrolyte reservoirs, significantly reducing diffusion resistance and enhancing rate capability, especially under high current densities [14–16]. Therefore, a synergistic combination of micropores and mesopores in porous carbon electrodes is essential for achieving both high capacitance and excellent power performance.

The conventional strategies for constructing porous carbon materials can generally be divided into activation methods and template-assisted methods, each possessing inherent advantages and limitations [17–23]. Activation methods, including chemical and physical activation, generate porosity through the etching and reconstruction of carbon frameworks. The chemical activation using corrosive agents, such as KOH and $ZnCl_2$, is highly effective in creating abundant micropores and achieving large SSA. However, these corrosive reagents often lead to severe

All rights reserved, including rights for text and data mining and training of artificial intelligence technologies or similar technologies.
© 2026 Wiley-VCH GmbH

equipment degradation, complicated post-treatment procedures, and increased production costs. The physical activation employing oxidizing gases or steam (e.g., CO_2 or H_2O) is relatively environmentally benign and industrially viable, but typically requires prolonged processing times, produces randomly distributed pores, and results in comparatively lower surface areas. In contrast, the template-assisted methods, employing either soft or hard templates, are able to precisely tailor the pore sizes and morphologies of the porous carbons. Nevertheless, the synthesis and subsequent removal of templates are generally complex and time-consuming, and the use of hazardous etchants (such as HF for silica removal) raises serious safety and environmental concerns. A more efficient and sustainable alternative strategy, self-templating method, has emerged recently, wherein porous carbons are generated through direct carbonization of suitable precursors without external templates. Although this approach minimizes the use of corrosive chemicals and simplifies the synthesis process, it still faces notable challenges: biomass-derived carbons commonly exhibit disordered and poorly controlled pore structures, while carbons obtained from metal–organic salts or related precursors often suffer from low carbon yields and limited SSA. Consequently, developing scalable and controllable strategies to construct hierarchical porous carbons with optimized micro-/mesopore architectures remains a key challenge for advancing high-performance supercapacitor electrodes.

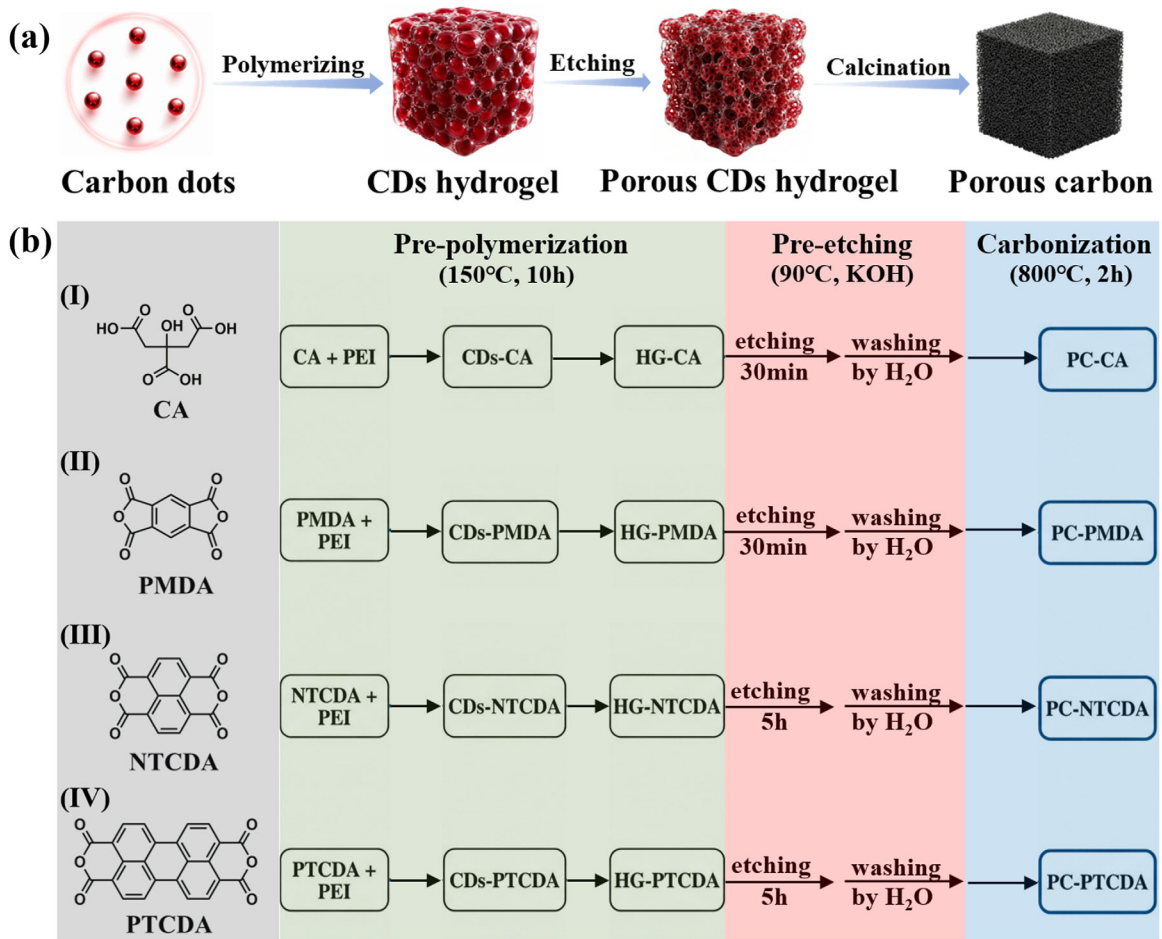
Recently, carbon dots (CDs), as an important class of zero-dimensional carbon nanomaterials, have been found as effective templates in the construction of porous carbon architectures, offering a fundamentally new paradigm for pore engineering [24–26]. Compared with conventional hard or soft templates, CDs exhibit several intrinsic advantages, including narrow size distributions, excellent dispersibility, and broad precursor availability [27–29]. Their surfaces are rich in tunable functional groups and defect sites, which readily undergo crosslinking, structural rearrangement, or partial decomposition during thermal treatment, thereby inducing the in situ formation of pores [30, 31]. In addition, CDs provide a versatile platform for heteroatom incorporation and electronic structure modulation of the carbon framework, which is beneficial for enhancing the electrochemical activity and structural stability of porous carbons [32–34]. In our previous studies, porous carbons with high SSA and pore size distributions narrowly centered in the sub-nanometer range (0.5–1.0 nm) were successfully synthesized using CDs as the sole precursor via a self-templated carbonization strategy, demonstrating the unique capability of CDs in constructing well-defined microporous structures [12]. However, the resulting pore architecture were almost monodispersed, and controllable expansion of pore sizes from narrow micropores to larger micropores was not achieved. Moreover, an excessively high proportion of micropores inevitably hampers rapid ion transport within the electrode, leading to limited rate performance at high current densities, a drawback that becomes particularly pronounced when bulky electrolyte ions are employed [35, 36]. Therefore, a systematic investigation on the pore formation and evolution mechanisms during CDs-based self-templating is of critical importance for elucidating the governing principles of pore-size enlargement and hierarchical pore construction, as well as overcoming the intrinsic limitations of CD-derived porous carbons in advanced energy storage applications ultimately.

In this study, we synthesized a series of CDs by employing four organic acids in combination with polyethyleneimine (PEI) as precursors, respectively. These acids have distinct molecular sizes and structures, that are citric acid (CA), pyromellitic dianhydride (PMDA), naphthalene-1,4,5,8-tetracarboxylic dianhydride (NTCDA) and perylene-3,4,9,10-tetracarboxylic dianhydride (PTCDA), respectively. By deliberately tuning the molecular architecture of the acid components, the chemical composition and crosslinking propensity of the resulting CDs could be systematically modulated. These molecularly designed CDs were subsequently employed as the sole carbonaceous building blocks in a pre-polymerization and pre-etching process, followed by carbonization to produce porous carbons without relying on conventional high-temperature activation with strongly corrosive activating agents. A comprehensive analysis of the resulting pore structures revealed a clear correlation between the intrinsic structural characteristics of the CDs and the final pore size distributions of the derived carbons. Combined with stepwise characterization of the pore formation process, these results allowed us to elucidate the underlying mechanism of pore generation driven by CDs self-templating and alkaline etching. Therefore, this research establishes an effective pathway for adjusting the distribution of mesopores and micropores just by changing CDs self-templates. Among the obtained samples, the material derived from PMDA-based CDs (denoted as PC-PMDA) exhibited the most balanced pore architecture, simultaneously featuring a high SSA and a substantial mesopore contribution. When evaluated in 6 M KOH electrolyte, PC-PMDA delivered an outstanding specific capacitance of 475 F g^{-1} at an ultrahigh current density of 60 A g^{-1}. More importantly, even at a commercially relevant electrode mass loading of 10 mg cm^{-2}, the electrode retained 78% of its capacitance relative to that at 1 mg cm^{-2}. Overall, this work not only provides the deeper mechanistic insight into the role of CDs in self-templated pore engineering, but also broadens their applicability as versatile and powerful precursors for the rational design of advanced porous carbons for high-performance energy storage devices.

2 | Results and Discussion

The synthetic procedure of the porous carbon is illustrated in Scheme 1, in which CDs act as crosslinking nodes, pore-generating agents, and heteroatom dopant sources concurrently. Initially, four acids with distinct molecular weights (CA, PMDA, NTCDA, and PTCDA) were individually subjected to hydrothermal treatment with PEI in an autoclave, leading to the formation of CDs. As the reaction proceeded under elevated temperature and pressure, it gradually transitioned into the pre-polymerization stage. Abundant functional groups on the CDs promoted extensive intermolecular crosslinking, leading to the formation of highly compact and mechanically robust hydrogels. This dense network effectively suppressed excessive mass loss during final thermal treatment. A subsequent pre-etching stage was implemented, where a mild alkaline solution was introduced to selectively cleave amide linkages within the carbon dot framework, enabling the controlled extraction of small molecular fragments. The crosslinked precursor network therefore needs to satisfy two competing requirements: sufficient connectivity to preserve a continuous carbon framework and sufficient etchability to permit controlled fragment removal. A

16136829, 0, Downloaded from https://onlinelibrary.wiley.com/doi/10.1002/smll.76319 by Huan-Ming Xiong - Fudan University , Wiley Online Library on [19/10/2026]. See the Terms and Conditions (https://onlinelibrary.wiley.com/terms-and-conditions) on Wiley Online Library for rules of use; OA articles are governed by the applicable Creative Commons License



SCHEME 1 | (a) Schematic diagram of the synthetic procedure of porous carbon. (b) Specific conditions for synthesizing four kinds of porous carbons, respectively.

weakly connected network may undergo excessive structural contraction or collapse during subsequent treatment, whereas an overly condensed network may limit the generation of precursor voids. The balance between framework retention and controlled etching is therefore considered an important factor in determining the evolution of hierarchical porosity. After a thorough washing to remove residual alkali and small fragments, numerous pores were generated in situ throughout the hydrogel matrix. The alkali-treated hydrogels were finally converted into porous carbons by direct carbonization without introducing any corrosive activating agents.

High-resolution transmission electron microscopy (HRTEM) images (Figure 1a–d) show that, the average diameters of CDs-CA, CDs-PMDA, CDs-NTCDA, and CDs-PTCDA are 2.7, 3.2, 12.1, and 18.6 nm, respectively, evidencing a pronounced size enlargement of CDs as their precursor molecular weights increase. This trend can be rationalized by a precursor-dependent nucleation–growth balance: smaller, highly soluble molecules (e.g., CA-type precursors) typically generate a higher density of nuclei and undergo rapid surface passivation, which kinetically constrains particle growth; in contrast, larger and more π-rich aromatic precursors tend to form more stable pre-condensed clusters and exhibit stronger π–π association during hydrothermal carbonization, thereby favoring coalescence and sustained lateral growth of sp^2 domains, ultimately yielding larger nanoparticles [37]. Additionally, distinct lattice fringes can be observed in all CDs, with an interplanar spacing of approximately 0.21 nm. This spacing is consistent with the characteristic spacing of the (100) plane of graphitic carbon, indicating that the obtained carbon nanodots are not completely amorphous but contain a certain degree of ordered sp^2 carbon domains or graphitic microcrystalline structures [38, 39]. This result suggests that condensation and rearrangement of aromatic structures occurred during the carbonization process, leading to the formation of graphitized carbon cores with short-range crystalline order [40]. The X-ray diffraction (XRD) patterns (Figure 1e) further support these conclusions: CDs-CA shows a broad diffuse peak spanning 15°–30°, indicative of a highly disordered carbon network with limited sp^2 domains, which is commonly associated with abundant O/N-containing functionalities [41]. By comparison, the remaining three CDs present a relatively sharper feature near 19° together with a left-shifted (002) reflection, implying the presence of short-range ordered graphitic-like stacking accompanied by interlayer expansion, in good agreement with the HRTEM observations.

Fourier transform infrared (FTIR) spectra (Figure 1f) of all CDs exhibit four characteristic bands at around 3443, 1629, 1387, and 1026 cm^{-1}, which are attributed to O–H/N–H stretching, C = C/C = O vibrations (including amide-related contributions), C–N stretching, and C–O stretching, respectively, confirming that all CDs are enriched with amide linkages, amine moieties,

16136829, 0, Downloaded from https://onlinelibrary.wiley.com/doi/10.1002/smll.76319 by Huan-Ming Xiong - Fudan University , Wiley Online Library on [19/10/2026]. See the Terms and Conditions (https://onlinelibrary.wiley.com/terms-and-conditions) on Wiley Online Library for rules of use; OA articles are governed by the applicable Creative Commons License

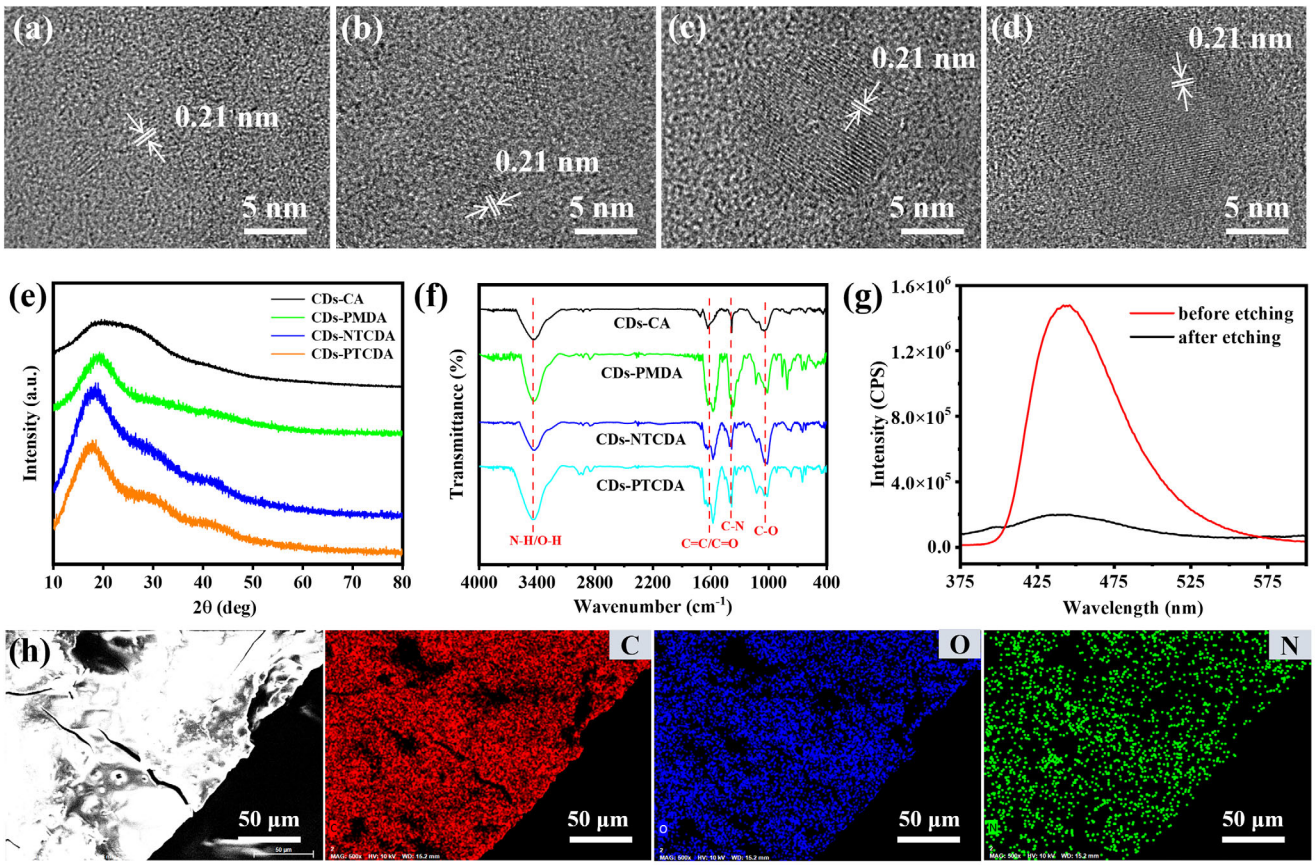


FIGURE 1 | HRTEM images of (a) CDs-CA, (b) CDs-PMDA, (c) CDs-NTCDA and (d) CDs-PTCDA, respectively. (e) XRD patterns and (f) FTIR spectra of the four kinds of CDs, respectively. (g) Fluorescence spectra of CDs-PMDA before and after etching. (h) EDS elemental mappings of C, N, and O elements in HG-PMDA hydrogel, respectively.

and oxygenated groups [42]. These surface reactive functionalities provide the chemical basis for the spontaneous self-polymerization of the CDs. Upon KOH treatment, cleavage of amide bonds and the concomitant generation of internal defects disrupt the emissive states, which is directly reflected by the marked fluorescence attenuation after etching (Figure 1g and Figure S1), consistent with partial destruction of conjugated domains. In order to evaluate the compositional uniformity of the self-polymerized hydrogel, energy-dispersive X-ray spectroscopy (EDS) mapping was conducted on the HG-PMDA hydrogel. As shown in Figure 1h, the signals for C, N, and O elements are homogeneously distributed throughout the matrix, corroborating the good compositional uniformity of the hydrogel network.

To elucidate the working principle of the pre-etching step, the morphologies of HG-CA, HG-PMDA, HG-NTCDA, and HG-PTCDA before and after etching were comparatively examined by SEM (Figure 2a–h and Figures S2 and S3) and TEM (Figures S4 and S5). In the pristine state, HG-CA exhibits a compact and compliant surface, whereas HG-PMDA appears as an assembly of fine particulates, which may be attributed to the dual nature of PMDA—an aromatic yet relatively small building unit—prone to localized cluster formation during gelation. By contrast, HG-NTCDA and HG-PTCDA display flatter, block-like surfaces. Notably, TEM images reveal dark-contrast lamellar aggregation domains with a "thick-and-stacked" appearance, consistent with locally densified regions and more ordered π-stacked motifs induced by larger polycyclic aromatic units.

After etching, HG-CA develops abundant, uniformly distributed fine pores, while HG-NTCDA and HG-PTCDA mainly show pronounced wrinkling accompanied by small fissures—an intuitive signature of partial network degradation and shrinkage. A distinct feature is observed for HG-PMDA, that numerous micron-scale cavities emerge. This behavior is plausibly linked to the cluster-forming tendency of PMDA-derived domains, which undergo a more "selective, patch-wise" removal during bond scission and leaching. Adjacent defects readily coalesce, amplifying into large pores. Meanwhile, the relatively rigid aromatic backbone in HG-PMDA can stabilize pore walls and help preserve the macropore geometry, allowing these large cavities to survive subsequent carbonization. In comparison, HG-NTCDA and HG-PTCDA contain larger fused aromatic cores, enhancing network rigidity and aromatic association, thereby impeding hydroxide penetration and rendering degradation slower and spatially more dispersed, which is consistent with the extended etching duration (5 h) required for these hydrogels. In addition, the dissolution of the etched-off fragments is more restricted when the released motifs are larger, suppressing further pore coalescence and limiting macropore growth. Conversely, although HG-CA is constructed from smaller structural units, its matrix is more hydrophilic and compositionally uniform and exhibits greater framework flexibility. As a result, etching tends to proceed more

16136829, 0, Downloaded from https://onlinelibrary.wiley.com/doi/10.1002/smll.76319 by Huan-Ming Xiong - Fudan University , Wiley Online Library on [19/10/2026]. See the Terms and Conditions (https://onlinelibrary.wiley.com/terms-and-conditions) on Wiley Online Library for rules of use; OA articles are governed by the applicable Creative Commons License

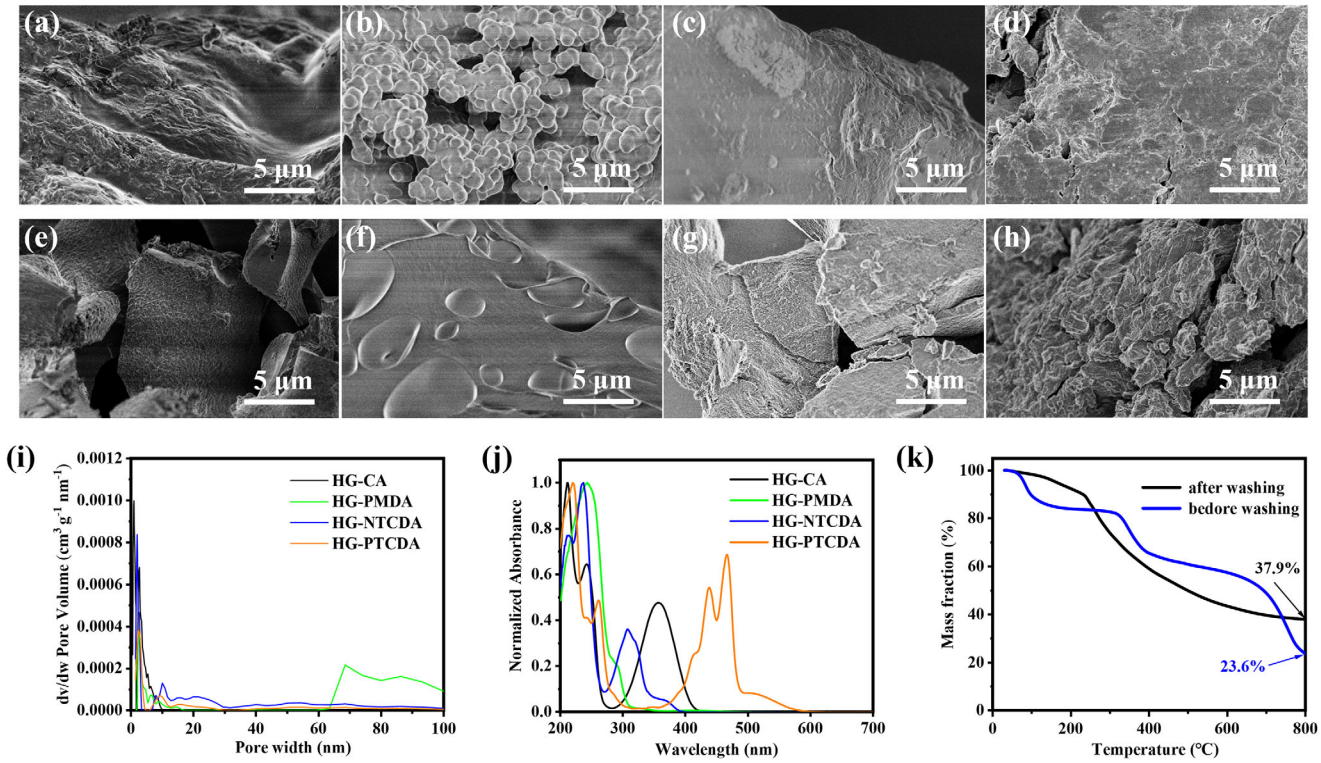


FIGURE 2 | SEM images of (a, e) HG-CA, (b, f) HG-PMDA, (c, g) HG-NTCDA and (d, h) HG-PTCDA, (a–d) before and (e–h) after etching, respectively. (i) Pore size distributions of all etched hydrogels. (j) UV–vis spectra of the leached fragments collected from different etched hydrogels, respectively. (k) TG curves of the etched HG-PMDA with and without washing treatment.

homogeneously, accompanied by local contraction and collapse, ultimately yielding a dense population of small, relatively uniform pores. This mechanistic picture agrees with the mass-loss trend, where HG-PMDA shows the largest mass decrease after etching, implying the most extensive node removal and leaching, which correlates with its most prominent macropore formation.

Consistent with the microscopy results, the pre-etched hydrogels are essentially nonporous, whereas nitrogen adsorption–desorption measurements show that the etched counterparts display pronounced uptake and pore architectures. The pore-size distribution (Figure 2i) indicates that all etched hydrogels develop abundant pores predominantly below 20 nm, suggesting that etching creates micro/mesoporous transport pathways through selective bond cleavage and subsequent elution of soluble fragments. The corresponding SSA are 8.2, 5.4, 2.4, and 1.1 $m^2\ g^{-1}$ for HG-CA, HG-PMDA, HG-NTCDA, and HG-PTCDA, respectively. Importantly, only HG-PMDA exhibits a clear contribution from large pores (>60 nm), in line with SEM and TEM observations and indicative of defect coalescence that produces a hierarchical pore system. Such a pore network is expected to serve as a preformed channel scaffold that can be "locked in" by the carbon framework during carbonization, enabling the resulting porous carbons to inherit, at least partially, the pore-size characteristics of their precursors.

To probe the chemical nature of the species released during etching, all leached fragments collected from the etched hydrogels were analyzed by UV–vis spectroscopy (Figure 2j). The band near 215 nm can be assigned to the superposition of the aromatic E band and the carbonyl $\pi \rightarrow \pi^*$ transition: aromatic rings typically exhibit a strong E2 band in the 200–215 nm region, while carbonyl groups in amides/carboxyls absorb strongly around 190–210 nm and can undergo a slight redshift when conjugated with aromatic moieties. The absorption within 235–260 nm corresponds to the characteristic B band of benzene-type chromophores. These signatures collectively indicate that the detached fragments from all samples retain aromatic motifs, indirectly supporting the presence of graphitized cores in the CDs. Notably, compared with the more discrete spectral features of other samples, the HG-PMDA leachate displays a markedly broadened absorption envelope across 200–300 nm, implying substantial structural heterogeneity, namely, the fragments possess a distribution of conjugation lengths and surface functionalities. This polydispersity broadens the distribution of electronic gaps, leading to extensive band overlap and macroscopic peak broadening. The HG-CA leachate shows a moderate absorption at 356 nm, consistent with an $n \rightarrow \pi^*$ transition associated with citric acid–amine condensation/cyclization products [43]. Additionally, small fragments can form hydrogen-bonded aggregates, further broadening this band. For HG-NTCDA, a weak feature at 307 nm and a subtle shoulder near 360 nm resemble the fingerprint absorptions of naphthalene-type skeletons with slight substituent-induced shifts [44]. HG-PTCDA exhibits a strong band around 450 nm with vibronic fine structure, characteristic of a highly conjugated pyrene-like chromophore whose main transition is strongly redshifted by intramolecular charge transfer (ICT) effects [45]. Together, these results support that the released fragments preserve structural elements derived from the four acid precursors, providing key evidence for the etching pathway.

16136829, 0, Downloaded from https://onlinelibrary.wiley.com/doi/10.1002/smll.76319 by Huan-Ming Xiong - Fudan University , Wiley Online Library on [19/10/2026]. See the Terms and Conditions (https://onlinelibrary.wiley.com/terms-and-conditions) on Wiley Online Library for rules of use; OA articles are governed by the applicable Creative Commons License

To verify the effectiveness of post-etch washing in removing residual base, HG-PMDA was further examined by thermogravimetric analysis (TGA). The thermogravimetric (TG) curve (Figure 2k) and derivative thermogravimetric (DTG) curve (Figure S6) of the hydrogel before washing display three pronounced rapid mass-loss regions at 50°C–144°C, 311°C–402°C, and 639°C–800°C. The low-temperature event is mainly associated with desorption of water retained by the strong hygroscopicity of KOH. The mid-temperature loss corresponds to the principal thermal decomposition of the hydrogel network and is sharpened by potassium salt [46]. The high-temperature loss is consistent with potassium-mediated secondary mass loss, in line with further activation of carbonaceous frameworks at elevated temperatures. In contrast, the thoroughly washed hydrogel shows only a gentle mass decrease below 232°C (release of minor adsorbed water), followed by the onset of the main decomposition. The mass-loss rate then decreases smoothly and approaches a stable plateau at 800°C, without the low-temperature hygroscopic step or the high-temperature activation-like rapid loss [47]. This clear difference confirms that residual alkali is effectively removed by washing. Collectively, all characterizations above support a pre-etching mechanism: KOH induces scission of amide linkages within CDs-derived junctions, generating soluble molecular fragments that are extracted during rinsing along with residual K species. The removal of these fragments introduces defects and interconnected voids throughout the hydrogel matrix, which then evolve into the corresponding micro/mesoporous structures during subsequent calcination.

The etched hydrogels were directly carbonized to afford the corresponding porous carbons, and their microstructures and pore features were systematically characterized. As shown in Figure 3, the porous carbons derived from different precursors exhibit markedly distinct morphologies after carbonization, underscoring that molecular-level precursor design and the pre-etching behavior play decisive roles in directing structural evolution of the final carbon frameworks. Specifically, PC-CA displays a three-dimensional interconnected network with continuous pore channels in SEM (Figure 3a), indicating good overall connectivity. TEM further reveals abundant, uniformly distributed pores (Figure 3b), suggesting that the fine pores generated homogeneously in HG-CA are effectively preserved during carbonization. In contrast, PC-PMDA exhibits the most pronounced hierarchical porosity. SEM images show numerous micron-sized cavities that are spatially interconnected, forming an open skeletal framework (Figure 3c). Meanwhile, TEM also confirms a dense population of micron-sized pores (Figure 3d). This hierarchical architecture can be directly traced to the selective node removal and defect coalescence occurring during the etching of HG-PMDA. The preformed micron-scale pores are mechanically supported by the relatively rigid aromatic backbone and thereby "locked in" during carbonization, enabling robust inheritance of the hierarchical pore motif in the resulting porous carbon.

A clear morphological transition is observed for PC-NTCDA. Its SEM image is dominated by compact, bulky domains with only limited pore features (Figure 3e). TEM corroborates a substantial decrease in pore numbers (Figure 3f), implying that a considerable fraction of the etching-induced pores becomes partially closed upon carbonization. This behavior is plausibly associated with the larger fused aromatic core of NTCDA-derived motifs, which promotes local structural rearrangement and densification during high-temperature treatment, thereby compromising pore formation. PC-PTCDA represents the most extreme case. SEM reveals predominantly smooth, stacked lamellar structures with scarcely any open channels (Figure 3g). Consistently, TEM shows thick, dark-contrast stacked domains with little discernible porosity (Figure 3h). These observations indicate that PTCDA-derived highly fused aromatic units tend to form dense carbon domains with strong π–π interactions during carbonization, leading to extensive annihilation of the limited pores introduced at the etching stage. Overall, these results demonstrate that the ultimate pore architecture of the porous carbon is not generated randomly during carbonization. Rather, it is strongly governed by the molecular configuration and network rigidity established at the hydrogel stage. In particular, PMDA-derived systems with moderate aromaticity and a propensity for localized aggregation are most favorable for constructing stably inheritable hierarchical porosity, whereas excessively large fused aromatic backbones and overly rigid networks tend to suppress pore formation and preservation. This comparative study further validates the effectiveness of the "molecular design–hydrogel structuring–pre-etching–carbonization inheritance" strategy for tailoring pore architectures, providing a viable route to controllable porous carbons without resorting to corrosive activation.

The XRD patterns of all porous carbons display two broad reflections at 2θ = 24.7° and 43.4°, which can be assigned to the (002) and (100) planes of turbostratic graphite-like carbon, respectively (Figure 4a). The pronounced peak broadening indicates dominant short-range ordering with limited long-range periodicity, which is characteristic of amorphous porous carbons [48]. Notably, the diffraction intensities of PC-PMDA, PC-NTCDA, and PC-PTCDA are overall higher than those of PC-CA. This difference can be rationalized by precursor aromaticity. PMDA, NTCDA, and PTCDA contain aromatic frameworks that promote stronger π–π interactions and local stacking already at the hydrogel stage, which facilitates aromatization and layer rearrangement during carbonization [49]. As a result, relatively larger graphite-like domains are formed, enhancing the X-ray reflections. In contrast, the CA-derived network lacks preorganized aromatic domains, leading to the smaller crystals and more disordered stacking, with the weakest XRD signals.

Raman spectra show the typical D band at 1333 cm^{-1} and G band at 1576 cm^{-1} (Figure 4b), associated with the defect-related vibrations and the graphitic sp^2 carbon stretching, respectively. A higher I_D/I_G ratio generally reflects a higher defect density and a lower degree of structural ordering, which is common for porous carbons with O/N heteroatom incorporation [50]. With increasing precursor aromaticity, I_D/I_G gradually decreases, indicating that aromatic units favor the formation of larger sp^2 conjugated domains during carbonization and reduce the relative contribution of edge defects [51]. This trend is consistent with the strengthened graphite-like features observed by XRD.

FTIR spectra reveal persistent absorptions attributable to N–H/O–H, C–O, and C–N functionalities in all samples (Figure 4c), confirming the retention of oxygenated and nitrogen-containing groups in the samples after carbonization. These polar functionalities can improve electrolyte wettability and provide additional pseudocapacitive contributions, which is beneficial for

16136829, 0, Downloaded from https://onlinelibrary.wiley.com/doi/10.1002/smll.76319 by Huan-Ming Xiong - Fudan University , Wiley Online Library on [19/10/2026]. See the Terms and Conditions (https://onlinelibrary.wiley.com/terms-and-conditions) on Wiley Online Library for rules of use; OA articles are governed by the applicable Creative Commons License

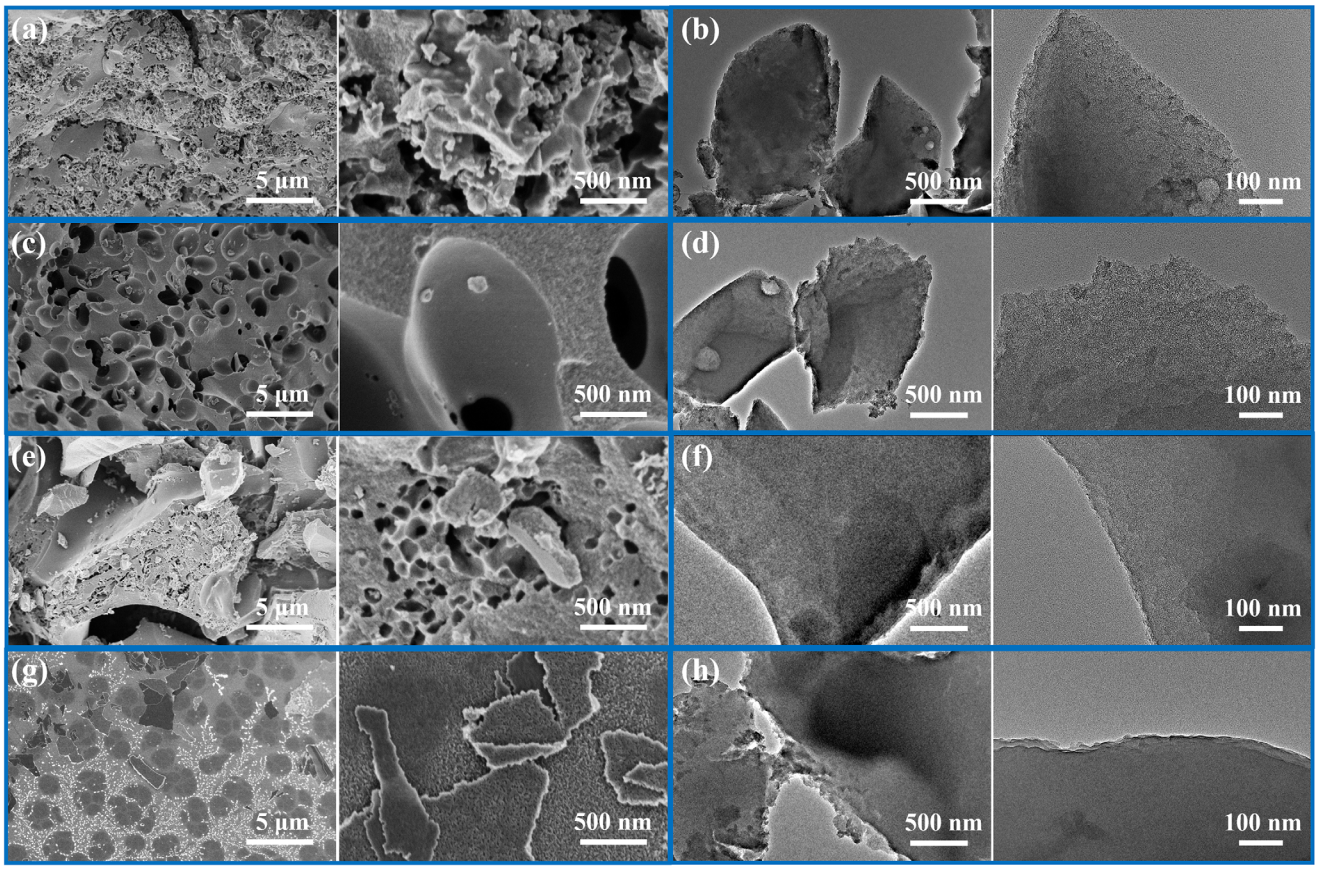


FIGURE 3 | SEM (left) and TEM (right) images of (a, b) PC-CA, (c, d) PC-PMDA, (e, f) PC-NTCDA and (g, h) PC-PTCDA, respectively.

electrochemical kinetics and rate capability [52, 53]. XPS analyses (Figure S7 and Table S1) further disclose the material compositions and electronic structures. All samples retain a relatively high oxygen content and a small amount of nitrogen, which can enhance hydrophilicity and introduce reversible redox-active sites, thus strengthening pseudocapacitive behavior [54–56]. The high-resolution N 1s spectra can be deconvoluted into pyridinic N, pyrrolic N, graphitic N, and oxidized N, respectively. The high fractions of pyridinic and pyrrolic species are commonly linked to electron-rich edge sites, which facilitate ion adsorption and insertion as well as interfacial charge transfer, improving ion storage and capacitive response. The O 1s spectra suggest the samples have similar oxygen speciation that are composed of C = O and C–O species. In particular, carbonyl or quinone-like sites can act as key pseudocapacitive centers by increasing surface reactivity and strengthening ion adsorption.

To elucidate the pore characteristics, N_2 adsorption and desorption measurements were conducted. The pore-size distributions show that the maximum distribution pore sizes of PC-CA, PC-PMDA, PC-NTCDA, and PC-PTCDA are 0.50, 0.79, 0.87, and 1.19 nm, respectively (Figure 4d). In light of the proposed "pre-etching and carbonization inheritance" mechanism, pre-etching primarily induces base-triggered cleavage of amide linkages at CDs-related junctions and leaches out soluble fragments, thereby creating vacancies and defects within the hydrogel network. Because the CA-derived matrix is built from smaller units and is more hydrophilic and compositionally uniform, etching proceeds more homogeneously and ultimately yields a dense population of narrowly distributed micropores after carbonization. As the aromatic dianhydride precursors become larger and more fused, both the spatial scale of the released fragments and the local network rigidity increase, so the hydrogels tend to leave wider microporous voids, giving rise to an increased characteristic pore size. However, in the NTCDA and PTCDA systems, strong π–π stacking and thermally driven rearrangement can partially close pore channels or merge them into thick stacked carbon domains. This leads to a coexistence of enlarged pore width and reduced pore number, which also explains the pronounced decrease in SSA. Regarding adsorption isotherms, PC-PMDA shows clear micropore filling at low relative pressure ($P/P_0 < 0.01$), while the overall profile resembles a type IV isotherm with an evident hysteresis loop (Figure S8), indicating a substantial mesoporous contribution and a hierarchical pore architecture. This observation agrees with the previously proposed pathway involving selective removal of PMDA-derived clustered domains, followed by defect coalescence and the generation of macro and mesopores. By comparison, the other three samples exhibit isotherms closer to type I, confirming predominantly microporous structures with limited mesoporosity. As summarized in Figure 4e,f and Table S2, the SSA values of PC-CA, PC-PMDA, PC-NTCDA, and PC-PTCDA are 2009, 1731, 1286, and 703 $m^2 \cdot g^{-1}$, respectively. This trend highlights the capability of the CDs self-templating strategy to construct high-SSA porous carbons without harsh chemical activation, while also indicating that excessively large molecular building blocks and overly rigid aromatic frameworks hinder deep etching and fragment dissolution. Consequently, defect coalescence and the formation of

16136829, 0, Downloaded from https://onlinelibrary.wiley.com/doi/10.1002/smll.76319 by Huan-Ming Xiong - Fudan University , Wiley Online Library on [19/10/2026]. See the Terms and Conditions (https://onlinelibrary.wiley.com/terms-and-conditions) on Wiley Online Library for rules of use; OA articles are governed by the applicable Creative Commons License

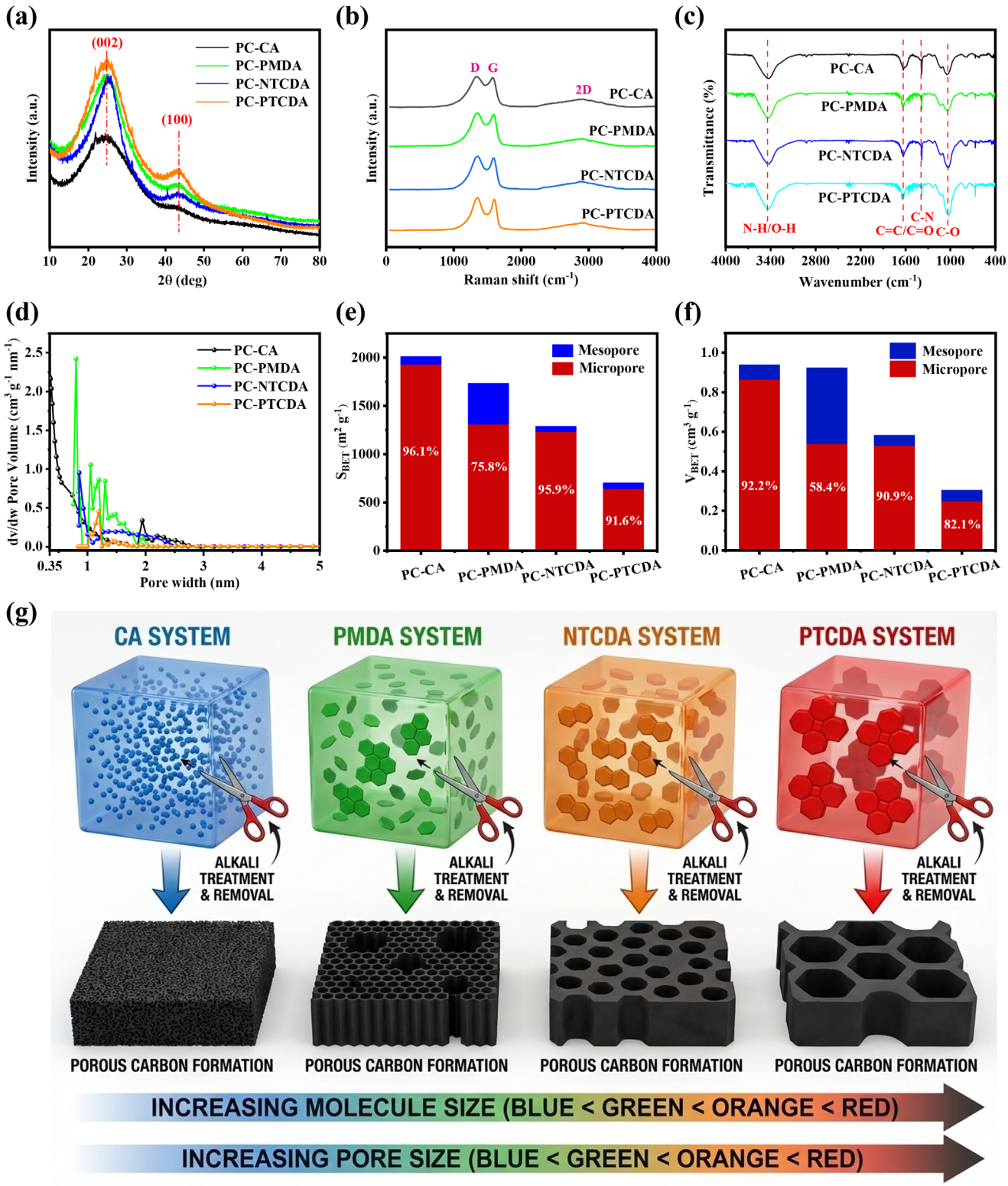


FIGURE 4 | (a) XRD, (b) Raman spectra, (c) FT-IR spectra, (d) pore size distributions, (e) specific surface areas, (f) specific pore volumes of all porous carbons, respectively. (g) Proposed formation mechanisms for porous carbons.

continuous transport channels are suppressed, and densification during carbonization becomes more pronounced, leading to fewer pores and lower SSA. The micropore volume fractions further support the pore-level differences. They are 92.2%, 58.4%, 90.9%, and 82.1% for PC-CA, PC-PMDA, PC-NTCDA, and PC-PTCDA, respectively. The markedly reduced micropore fraction of PC-PMDA reflects that it has more rapid transport pathways, which goes beyond the conventional notion that CDs self-templating mainly yields microporous carbons. Such a hierarchical pore network is expected to lower diffusion resistance while maintaining high SSA, thereby benefiting high-rate electrochemical processes.

16136829, 0, Downloaded from https://onlinelibrary.wiley.com/doi/10.1002/smll.76319 by Huan-Ming Xiong - Fudan University , Wiley Online Library on [19/10/2026]. See the Terms and Conditions (https://onlinelibrary.wiley.com/terms-and-conditions) on Wiley Online Library for rules of use; OA articles are governed by the applicable Creative Commons License

Based on these results, a formation mechanism for porous carbon is proposed (Figure 4g). First, during pre-polymerization, CDs self-assemble and crosslink under hydrothermal conditions to form mechanically robust hydrogels that provide a continuous scaffold and etchable junctions. Second, during pre-etching, alkaline conditions preferentially cleave amide bonds at CDs-related junctions and extract soluble fragments, generating vacancy defects that progressively evolve into interconnected micro- and mesoporous channels. The CA, NTCDA, and PTCDA systems undergo more uniform etching and mainly yields dense micropores, whereas the PMDA system, owing to the combined features of aromatic clustering and small molecular size, more readily experiences selective domain removal and defect coalescence, producing meso- and macroporous skeletons that can be effectively locked in upon carbonization. In addition, the increased aromaticity of the precursor led to the difficulty of etching, resulting in a decrease in the SSA of the final porous carbon. Third, during high-temperature carbonization, the aromatic backbone promotes structural inheritance, but overly large fused aromatic units in the NTCDA and PTCDA systems intensify stacking thickening and densification, which partially close pores. Meanwhile, the larger the molecular weight of the precursor, the more the maximum pore diameter of the porous carbon will shift toward a higher value. Consequently, among the present carbon series, PC-PMDA exhibits a particularly favorable combination of substantial internal surface area and pronounced mesoporous contribution. Unlike PC-CA, whose pore volume is strongly dominated by micropores, and PC-NTCDA/PC-PTCDA, which show progressively reduced SSA, PC-PMDA retains a high SSA while developing a substantially more hierarchical pore distribution. This structural balance provides both extensive charge-storage surface and improved geometrical accessibility to the internal pore network, forming the structural basis for its high-rate electrochemical behavior.

Electrochemical evaluation of the porous carbon electrodes was performed in a three-electrode configuration using 6 M KOH aqueous electrolyte (Figure 5a–e and Figure S9–S12). Cyclic voltammetry (CV), galvanostatic charge and discharge (GCD), and electrochemical impedance spectroscopy (EIS) were employed to probe charge storage behavior and ion transport. At a scan rate of 50 mV s^{-1}, all electrodes delivered nearly rectangular CV profiles with a faint, reversible hump (Figure 5a), indicating that the capacitance is dominated by EDLC processes with an additional, small pseudocapacitive contribution. This extra capacitance is reasonably attributed to fast and reversible redox reactions associated with nitrogen and oxygen functionalities and to improved surface wettability in alkaline media, which facilitates the ingress and egress of hydrated ions within the pore network [57]. Notably, PC-PMDA exhibited the largest enclosed CV area, even though its SSA is slightly lower than that of PC-CA. This apparent inconsistency can be rationalized by considering pore accessibility and kinetics rather than surface area alone. An excessively high fraction of micropores can impose diffusion limitations and increase tortuosity, which leads to incomplete utilization of the internal surface under practical time scales. In contrast, a higher mesopore content in PC-PMDA provides ion-buffering reservoirs and short diffusion pathways to adjacent micropores, thereby improving rate capability. In other words, hierarchical porosity can outperform purely microporous structures because the "effective" surface participating in charge storage becomes larger when transport is accelerated.

GCD curves recorded at 1 A g^{-1} (Figure 5b) are close to isosceles triangles, supporting highly reversible capacitive behavior with minimal polarization. The gravimetric specific capacitances derived from these curves are 377 F g^{-1} for PC-CA, 582 F g^{-1} for PC-PMDA, 250 F g^{-1} for PC-NTCDA, and 135 F g^{-1} for PC-PTCDA. The CV responses at increasing scan rates (Figure 5c and Figure S9) and the GCD profiles at elevated current densities (Figure 5d and Figure S10) remain largely rectangular and symmetric, respectively, confirming efficient ion adsorption and desorption with good electrochemical reversibility. Rate performance, summarized by capacitance retention versus current density (Figure 5e and Figure S11a), further highlights the advantage of PC-PMDA. Even at 60 A g^{-1}, PC-PMDA maintains a high capacitance of 475 F g^{-1} with a small internal resistance (IR drop of 0.09 V), consistent with fast ion and electron transport enabled by its mesopore-enriched architecture. Long-term cycling stability was assessed for PC-PMDA at 5 A g^{-1} (Figure 5f). After 10 000 cycles, PC-PMDA retains 91% of its initial capacitance and maintains Coulombic efficiency close to 100%, demonstrating robust electrochemical durability. Benchmarking against representative porous carbon electrodes reported in the literature (Table S3) further supports the competitive performance of PC-PMDA. Importantly, practical applicability was examined by increasing the electrode mass loading from 1 to 10 mg cm^{-2} (Figure S11b–d). Under this more demanding condition, PC-PMDA still preserves 78% of its capacity, corresponding to 453 F g^{-1}, and exhibits excellent stability by retaining 97% of the initial capacitance after 10 000 cycles at 5 A g^{-1}.

EIS was used to quantify transport kinetics and resistance components. As shown in Figure S12a, Nyquist plots display a near-vertical line in the low-frequency region that approaches ideal capacitive behavior, while a semicircle at high frequency reflects combined interfacial and internal resistances. The fitted impedance parameters in Table S4 indicate that porous carbons derived from aromatic precursors generally possess lower resistance, which can be associated with higher electronic conductivity arising from more ordered carbon domains and improved electrode continuity. The Bode plots (Figure S12b) show phase angles close to −90° at low frequency, again consistent with capacitive characteristics. The characteristic relaxation time constant (τ_0), calculated from f_0 defined as the frequency at which the capacitance drops to half of its maximum value, follows the same trend and supports faster dynamic response for the lower-resistance samples.

A symmetric supercapacitor (SSC) was assembled using the best-performing PC-PMDA as electrodes, and its electrochemical behavior was evaluated in aqueous electrolytes of 6 M KOH and 1 M Na_2SO_4. As summarized in Figure 6a,b and Figure S13a, the gravimetric capacitance derived from GCD profiles reaches 113 F g^{-1} in KOH and 154 F g^{-1} in Na_2SO_4 at 1 A g^{-1}. When the current density increases to 10 A g^{-1}, the device still delivers 102 F g^{-1} in KOH and 117 F g^{-1} in Na_2SO_4, demonstrating excellent rate capability in both media. The GCD traces remain close to symmetric triangles over a broad range of current densities, which indicates highly reversible charge storage and consistently high Coulombic efficiency. The small polarization

16136829, 0, Downloaded from https://onlinelibrary.wiley.com/doi/10.1002/smll.76319 by Huan-Ming Xiong - Fudan University , Wiley Online Library on [19/10/2026]. See the Terms and Conditions (https://onlinelibrary.wiley.com/terms-and-conditions) on Wiley Online Library for rules of use; OA articles are governed by the applicable Creative Commons License

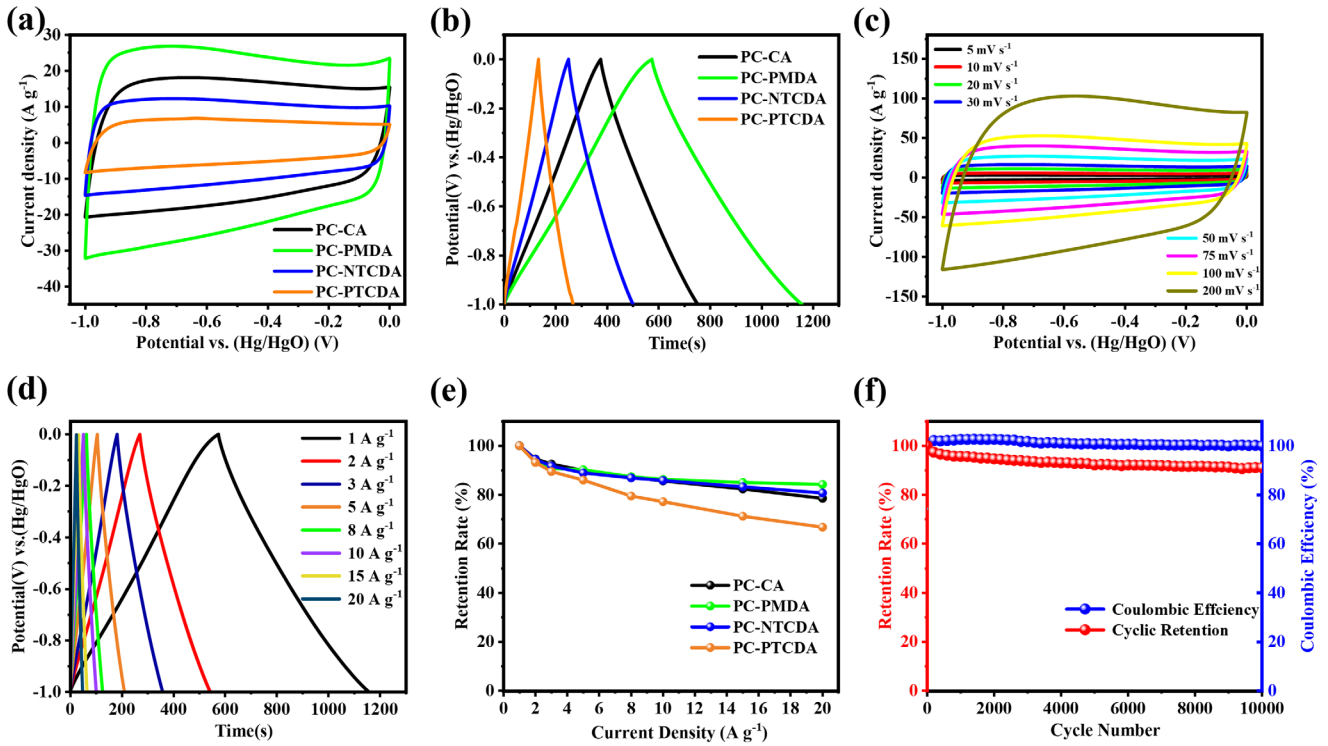


FIGURE 5 | Electrochemical performances tested via a three-electrode system. (a) CV curves at scan rates of 50 mV s^{-1} and (b) GCD curves at 1 A g^{-1} of all samples. (c) CV curves of PC-PMDA at various scan rates. (d) GCD curves of PC-PMDA at various current densities. (e) The rate performance at various current densities of all samples. (f) Cycling stability and Coulombic efficiencies of PC-PMDA for 10 000 cycles at 5 A g^{-1}.

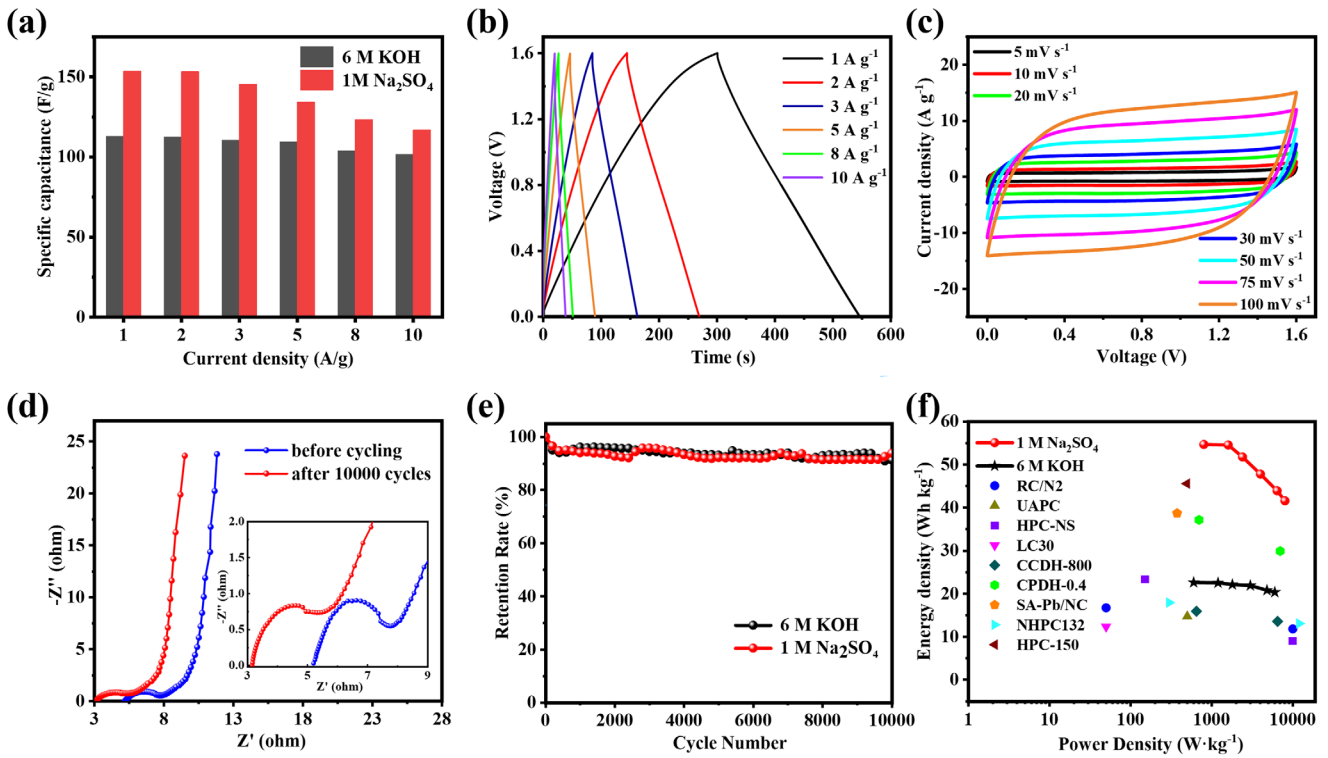


FIGURE 6 | Electrochemical performances of the PC-PMDA||PC-PMDA symmetric supercapacitor. (a) Specific capacitance in different electrolytes. (b) GCD curves at different current densities, (c) CV curves at various scan rates and (d) Nyquist plots before and after 10 000 cycles in 1 M Na_2SO_4 electrolyte. (e) Cycling stability at 3 A g^{-1} after 10 000 cycles. (f) Ragone plot of power density vs. energy density for PC-PMDA||PC-PMDA and other carbon-based symmetric devices.

16136829, 0, Downloaded from https://onlinelibrary.wiley.com/doi/10.1002/smll.76319 by Huan-Ming Xiong - Fudan University , Wiley Online Library on [19/10/2026]. See the Terms and Conditions (https://onlinelibrary.wiley.com/terms-and-conditions) on Wiley Online Library for rules of use; OA articles are governed by the applicable Creative Commons License

during charge and discharge is consistent with rapid ion migration through the hierarchical pore network of PC-PMDA and efficient electron transport within the carbon framework. CV tests further support this conclusion. As shown in Figure 6c and Figure S13b, the CV curves retain a well-defined quasi-rectangular outline as the scan rate increases, and they remain largely rectangular even at 100 mV s^{-1}. This behavior reflects low internal resistance and fast ion adsorption and desorption at the electrode. The combination of micropores and mesopores in PC-PMDA is expected to be particularly beneficial at high rates, since mesopores act as ion-buffering highways that shorten diffusion distances to adjacent micropore surfaces where charge is stored.

EIS tests provide complementary kinetic insight. The Nyquist plots (Figure 6d and Figure S13c) show a small semicircle in the high-frequency domain and an almost vertical line at low frequencies, confirming favorable charge-transfer dynamics and typical EDLC features. After 10 000 charge–discharge cycles, the diameter of the high-frequency semicircle changes only slightly and the low-frequency branch remains steep, indicating that the conductive network and pore architecture are well preserved during repeated operation. Long-term durability was quantified by GCD cycling. At 3 A g^{-1}, the SSC retains 91% of its initial capacitance in 6 M KOH and 94% in 1 M Na_2SO_4 after 10 000 cycles (Figure 6e), demonstrating excellent cycling life and robust reversibility. The device also exhibits attractive energy and power characteristics. The maximum energy density reaches 22.6 Wh kg^{-1} in alkaline electrolyte and increases to 54.6 Wh kg^{-1} in neutral electrolyte, which can be attributed to the wider stable operating voltage typically accessible in Na_2SO_4-based aqueous systems. Notably, even at a high power density of 8000 W kg^{-1}, the neutral-electrolyte device maintains a high energy density of 41.6 Wh kg^{-1}. These metrics compare favorably with many previously reported carbon-based supercapacitors operating in either alkaline or neutral aqueous electrolytes (Figure 6f), highlighting the practical potential of PC-PMDA for high-rate and high-energy aqueous energy storage [12, 34, 58–65].

3 | Conclusion

We report a controllable CDs self-templating route to hierarchical porous carbons by integrating rational CDs design with a pre-polymerization and pre-etching process, avoiding conventional high-temperature chemical activation while tuning the pore-architecture. By selecting organic acids with distinct molecular sizes and conjugation degrees together with polyethyleneimine, the composition and crosslinking propensity of CDs are systematically modulated, which dictates pore formation and evolution during alkaline etching and carbonization. Stepwise characterization establishes a clear structure–pore correlation and uncovers an efficient mechanism to introduce a substantial mesopore fraction into CDs-derived carbons, overcoming the limitation of narrowly distributed micropores. Benefiting from the balanced micro/mesoporosity, PC-PMDA achieves fast ion transport and robust EDLC performance, delivering 475 F g^{-1} at 60 A g^{-1} (IR drop of 0.09 V) and 91% of capacitance retention after 10 000 cycles at 5 A g^{-1}. Symmetric supercapacitors based on PC-PMDA provide high energy densities of 22.6 Wh kg^{-1} (in 6 M KOH) and 54.6 Wh kg^{-1} (in 1 M Na_2SO_4) with excellent durability. Overall, this work offers a mechanism insight and a general design principle for expanding pore sizes and constructing hierarchical porosity of carbon materials, developing the high-rate and high-energy electrodes for practical aqueous supercapacitors.

4 | Experimental Section

4.1 | Chemicals and Materials

Citric acid (CA), pyromellitic dianhydride (PMDA), naphthalene-1,4,5,8-tetracarboxylic dianhydride (NTCDA), perylene-3,4,9,10-tetracarboxylic dianhydride (PTCDA), ethylene imine polymer (PEI) and polytetrafluoroethylene preparation (PTFE) were obtained from Aladdin Reagent Co. (China). Hydrochloric acid, acetic acid, super P, and potassium hydroxide were purchased from Sinopharm Chemical Reagent Co., Ltd (Shanghai, China).

4.2 | Synthesis of CA-Based Hydrogel (HG-CA)

CA (8 mmol) and PEI (1 g) were dissolved in deionized water (6 mL). The resulting solution was transferred into a Teflon-lined stainless-steel autoclave and heated at 150°C. To probe the reaction evolution, a portion of the reaction mixture was withdrawn after 1 h; after dialysis and drying, carbon dots were obtained and denoted as CD-CA. The remaining samples were maintained under the same conditions for a total of 10 h, yielding a uniform hydrogel. The as-formed hydrogel was thoroughly washed with deionized water and dried at 80°C, and the product was designated as HG-CA.

4.3 | Synthesis of CA-Based Porous Carbon (PC-CA)

The obtained HG-CA hydrogel was immersed in 20 mL of 2 M KOH aqueous solution and treated at 90°C for 30 min to induce chemical etching. Afterward, the sample was repeatedly rinsed with deionized water and dried again at 80°C. The dried material was then carbonized in a tube furnace by heating to 300°C at a rate of 5°C min^{-1} and holding for 1 h, followed by further heating to 800°C at 2°C min^{-1} with a dwell time of 2 h under a nitrogen atmosphere. After natural cooling, the product was washed with deionized water and dried at 80°C, affording porous carbon powder, denoted as PC-CA.

4.4 | Synthesis of PMDA-Based Hydrogel (HG-PMDA)

PMDA (8 mmol) and PEI (1 g) were dissolved in deionized water (4 mL), followed by the addition of acetic acid (2 mL) under stirring to obtain a homogeneous solution. The mixture was then transferred into a Teflon-lined stainless-steel autoclave and heated at 150°C. To monitor the reaction progress, a portion of the reaction mixture was withdrawn after 1 h; carbon dots (CD-PMDA) were obtained after dialysis and drying. The remaining samples were further heated for a total of 10 h, leading to the formation of a uniform hydrogel, which was washed with deionized water and dried at 80°C, denoted as HG-PMDA.

16136829, 0, Downloaded from https://onlinelibrary.wiley.com/doi/10.1002/smll.76319 by Huan-Ming Xiong - Fudan University , Wiley Online Library on [19/10/2026]. See the Terms and Conditions (https://onlinelibrary.wiley.com/terms-and-conditions) on Wiley Online Library for rules of use; OA articles are governed by the applicable Creative Commons License

4.5 | Synthesis of PMDA-Based Porous Carbon (PC-PMDA)

HG-PMDA was etched in 20 mL of 2 M KOH aqueous solution at 90°C for 30 min, followed by thorough rinsing with deionized water and drying at 80°C. The sample was subsequently carbonized in a tube furnace by heating to 300°C at 5°C min^{-1} for 1 h and then to 800°C at 2°C min^{-1} for 2 h under a nitrogen atmosphere. After natural cooling, the product was washed and dried to yield porous carbon powder, designated as PC-PMDA.

4.6 | Synthesis of NTCDA-Based Hydrogel (HG-NTCDA)

NTCDA (8 mmol) and PEI (1 g) were dissolved in deionized water (4 mL), followed by the addition of acetic acid (2 mL) under stirring to obtain a homogeneous solution. The mixture was then transferred into a Teflon-lined stainless-steel autoclave and heated at 150°C. To monitor the reaction progress, a portion of the reaction mixture was withdrawn after 1 h; carbon dots (CD-NTCDA) were obtained after dialysis and drying. The remaining samples were further heated for a total of 10 h, leading to the formation of a uniform hydrogel, which was washed with deionized water and dried at 80°C, denoted as HG-NTCDA.

4.7 | Synthesis of NTCDA-Based Porous Carbon (PC-NTCDA)

HG-NTCDA was etched in 20 mL of 2 M KOH aqueous solution at 90°C for 5 h, followed by thorough rinsing with deionized water and drying at 80°C. The sample was subsequently carbonized in a tube furnace by heating to 300°C at 5°C min^{-1} for 1 h and then to 800°C at 2°C min^{-1} for 2 h under a nitrogen atmosphere. After natural cooling, the product was washed and dried to yield porous carbon powder, designated as PC-NTCDA.

4.8 | Synthesis of PTCDA-Based Hydrogel (HG-PTCDA)

PTCDA (8 mmol) and PEI (1 g) were dissolved in deionized water (4 mL), followed by the addition of acetic acid (2 mL) under stirring to obtain a homogeneous solution. The mixture was then transferred into a Teflon-lined stainless-steel autoclave and heated at 150°C. To monitor the reaction progress, a portion of the reaction mixture was withdrawn after 1 h; carbon dots (CD-PTCDA) were obtained after dialysis and drying. The remaining samples were further heated for a total of 10 h, leading to the formation of a uniform hydrogel, which was washed with deionized water and dried at 80°C, denoted as HG-PTCDA.

4.9 | Synthesis of PTCDA-Based Porous Carbon (PC-PTCDA)

HG-PTCDA was etched in 20 mL of 2 M KOH aqueous solution at 90°C for 5 h, followed by thorough rinsing with deionized water and drying at 80°C. The sample was subsequently carbonized in a tube furnace by heating to 300°C at 5°C min^{-1} for 1 h and then to 800°C at 2°C min^{-1} for 2 h under a nitrogen atmosphere. After natural cooling, the product was washed and dried to yield porous carbon powder, designated as PC-PTCDA.

4.10 | Electrochemical Measurements

Electrode films were prepared by homogenizing the as-obtained porous carbon with Super P and a PTFE binder in an 8:1:1 weight ratio. The slurry was then pressed onto a stainless-steel mesh current collector (geometric area: 1 cm^2) and dried at 80°C for 24 h to remove residual moisture and ensure mechanical integrity. The resulting electrodes exhibited an active-material loading of 1 or 10 mg cm^{-2}. Electrochemical characterization was performed in a three-electrode cell employing the Hg/HgO reference electrode and the platinum foil as counter electrodes, with 6 M KOH serving as the aqueous electrolyte. All measurements were conducted within a potential window of −1.0 to 0 V. For device-level evaluation, symmetric supercapacitors (SSCs) were assembled by pairing two identically prepared PC-PMDA electrodes. They were tested in 6 M KOH over an operating cell voltage of 0–1.2 V and in 1 M Na_2SO_4 over an operating cell voltage of 0–1.6 V. Cyclic voltammetry (CV) and electrochemical impedance spectroscopy (EIS) were collected on a CHI 660E electrochemical workstation, with EIS acquired over 0.01–100 kHz. Galvanostatic charge–discharge (GCD) experiments were carried out using a CT2001A LAND battery test system. The gravimetric capacitance (C_s) was derived from the GCD discharge profiles using the equation provided below:

$$C_s = \frac{I\Delta t}{m\Delta V} \tag{1}$$

where I (A), ΔV (V) and Δt (s) refer to the applied constant current, voltage window, and discharge time, respectively. Notably, m (g) is defined according to the testing configuration: for the three-electrode measurements, m is the active-material mass deposited on the working electrode, whereas for the SSCs m is taken as the total active-material mass from two electrodes.

The energy density (E_g, Wh kg^{-1}) and power density (P_g, W kg^{-1}) were determined using the equations provided below:

$$E_g = \frac{1}{2 \times 3.6} C_s \Delta V^2 \tag{2}$$

$$P_g = \frac{E_g \times 3600}{\Delta t} \tag{3}$$

Author Contributions

Xi-Rong Zhang: conceptualization, methodology, software, data curation, investigation, validation, formal analysis, visualization, writing – original draft. **Hao-Wen Sun**: data curation, investigation, validation, formal analysis. **Ling Xiao**: data curation, investigation, formal analysis. **Yong-Gang Wang**: supervision, funding acquisition, project administration, resources. **Huan-Ming Xiong**: conceptualization, methodology,

16136829, 0, Downloaded from https://onlinelibrary.wiley.com/doi/10.1002/smll.76319 by Huan-Ming Xiong - Fudan University , Wiley Online Library on [19/10/2026]. See the Terms and Conditions (https://onlinelibrary.wiley.com/terms-and-conditions) on Wiley Online Library for rules of use; OA articles are governed by the applicable Creative Commons License

funding acquisition, project administration, supervision, resources, writing – review and editing.

Acknowledgements

This work was financially supported by the National Natural Science Foundation of China (U24A20565, 22575057), the Science and Technology Commission of Shanghai Municipality (25ZR1401024).

Conflicts of Interest

The authors declare no conflicts of interest.

Data Availability Statement

The data that support the findings of this study are available from the corresponding author upon reasonable request.

References

1. J. X. Peng, T. Z. Wu, L. Zeng, Z. Liu, S. Q. Li, and G. Feng, "Realistic Atomic Model for Charge Storage and Charging Dynamics of Amorphous Porous Carbons," *Nature Communications* 17 (2026): 2425, https://doi.org/10.1038/s41467-026-69231-4.

2. M. K. Li, Z. Z. Shen, S. Shi, R. Wen, and B. Liu, "Engineering Freestanding Porous Carbon Electrodes by Self-Assembled Colloidal Liquid Crystalline Phase," *Journal of the American Chemical Society* 148 (2026): 11009–11019, https://doi.org/10.1021/jacs.5c22053.

3. H. L. Zhu, S. S. Qiu, M. J. Sun, et al., "Heterophasic Cobalt Sulfide Heterogeneous Interfaced Carbon Nanospheres With Enhanced Electromagnetic Wave Absorption And Thermal Insulation Performance," *Advanced Energy Materials* 263 (2026): 200–210, https://doi.org/10.1002/aenm.70821.

4. C. Ania, T. J. Bandosz, D. Cazorla-Amoros, and M. F. R. Pereira, "Advancing Porous Carbons: Understanding the Importance of Surface Chemistry for the Energy–Environment Nexus," *Chemical Reviews* 126 (2026): 2678–2800, https://doi.org/10.1021/acs.chemrev.5c00719.

5. J. K. Zhang, S. Li, Y. T. Feng, X. S. Zhao, Y. Qin, and J. L. Hu, "An In Situ Interfacial Assembly Approach to Synthesize a Functional Hierarchical Porous Carbon Nanoreactor With Surface-Confined Platinum," *ACS Nano* 20 (2026): 8803–8811, https://doi.org/10.1021/acsnano.5c22265.

6. Y. Gogotsi, A. Nikitin, H. H. Ye, et al., "Nanoporous Carbide-Derived Carbon With Tunable Pore Size," *Nature Materials* 2 (2003): 591–594, https://doi.org/10.1038/nmat957.

7. Y. T. Song, S. C. Fan, Z. R. Yan, et al., "Integrated Performance Metrics of Porous Carbon Toward Practical Supercapacitor Devices," *Nano-Micro Letters* 18 (2026): 219, https://doi.org/10.1007/s40820-026-02069-z.

8. T. Kress, X. Y. Liu, and A. C. Forse, "Pore Network Tortuosity Controls Fast Charging in Supercapacitors," *Nature Materials* 25 (2026): 440–446, https://doi.org/10.1038/s41563-025-02404-6.

9. C. Wang, X. X. Cheng, K. H. Luo, et al., "A Guided Review of Machine Learning in the Design and Application for Pore Nanoarchitectonics of Carbon Materials," *Materials Science and Engineering: R: Reports* 165 (2025): 101010, https://doi.org/10.1016/j.mser.2025.101010.

10. Z. X. Wang, T. Z. Wu, L. Zeng, et al., "High-Density Three-Dimensional Graphene Cathode With a Tailored Pore Structure For High Volumetric Capacity Zinc-Ion Storage," *Advanced Materials* 37 (2025): 202500943.

11. Y. T. Li, Q. Q. Li, S. Zhang, et al., "Application-Oriented Design of Microporous Carbons for Advanced Supercapacitors: From Fundamental Mechanisms to Rational Material Engineering," *Advanced Functional Materials* 36 (2026): 21004, https://doi.org/10.1002/adfm.202521004.

12. X. R. Zhang, B. J. Wang, H. W. Sun, Y. G. Wang, and H. M. Xiong, "Pre-Polymerization and Pre-Etching Dominated by Carbon Dots to Fabricate the Sub-Nanometer Microporous Carbon for Supercapacitors," *Angewandte Chemie International Edition* 64 (2025): 202519704, https://doi.org/10.1002/anie.202519704.

13. J. Q. Wei, L. X. Zhong, H. R. Xia, et al., "Metal-Ion Oligomerization Inside Electrified Carbon Micropores and its Effect on Capacitive Charge Storage," *Advanced Materials* 34 (2022): 2107439, https://doi.org/10.1002/adma.202107439.

14. X. Cai, K. X. Zhang, W. X. Chen, and X. Q. Hu, "Deciphering the Capacitive Behavior of Heteroatom–Doped Carbon Materials With Small Mesopores," *Energy Storage Materials* 82 (2025): 104584, https://doi.org/10.1016/j.ensm.2025.104584.

15. J. Park, K. Kim, E. Lim, and J. Hwang, "Tuning Internal Accessibility via Nanochannel Orientation of Mesoporous Carbon Spheres for High-Rate Potassium-Ion Storage in Hybrid Supercapacitors," *Advanced Functional Materials* 35 (2025): 2410010, https://doi.org/10.1002/adfm.202410010.

16. C. L. Liang, J. L. Fu, S. D. Tang, et al., "Unlocking Fast Charging of Supercapacitors: A Job-Sharing Mechanism for Ion Transport and Storage," *Energy Storage Materials* 83 (2025): 104685, https://doi.org/10.1016/j.ensm.2025.104685.

17. V. Pavlenko, S. Khosravi, S. Zoltowska, et al., "A Comprehensive Review of Template-Assisted Porous Carbons: Modern Preparation Methods and Advanced Applications," *Materials Science and Engineering: R: Reports* 149 (2022): 100682, https://doi.org/10.1016/j.mser.2022.100682.

18. V. Malgras, J. Tang, J. Wang, et al., "Fabrication of Nanoporous Carbon Materials With Hard- and Soft-Templating Approaches: A Review," *Journal of Nanoscience and Nanotechnology* 19 (2019): 3673–3685, https://doi.org/10.1166/jnn.2019.16745.

19. L. Sun, Y. N. Gong, D. L. Li, and C. X. Pan, "Biomass-Derived Porous Carbon Materials: Synthesis, Designing, and Applications for Supercapacitors," *Green Chemistry* 24 (2022): 3864–3894, https://doi.org/10.1039/D2GC00099G.

20. S. Li, H. Zhang, S. Li, J. Q. Wang, Q. W. Wang, and Z. L. Cheng, "Engineering Nanostructured Silicon and its Practical Applications in Lithium-Ion Batteries: A Critical Review," *Renew Sust Energy Rev* 202 (2024): 114641.

21. R. W. Fu, Z. H. Li, Y. R. Liang, F. Li, F. Xu, and D. C. Wu, "Hierarchical Porous Carbons: Design, Preparation, and Performance in Energy Storage," *New Carbon Materials* 26 (2011): 171–179, https://doi.org/10.1016/S1872-5805(11)60074-7.

22. T. Wang, P. X. Ren, Q. Liu, et al., "Coal Tar Pitch-Based Porous Carbon: Synthetic Strategies and Their Applications in Energy Storage," *Advanced Functional Materials* 36 (2026): 04092, https://doi.org/10.1002/adfm.202504092.

23. M. Sevilla, N. Díez, and A. B. Fuertes, "More Sustainable Chemical Activation Strategies for the Production of Porous Carbons," *Chemsuschem* 14 (2021): 94–117, https://doi.org/10.1002/cssc.202001838.

24. H. F. Yang, J. D. Hong, L. X. Wei, and C. L. Deng, "Synthesis of Hydroxyapatite Nanoparticles Using Surface Carboxyl-Functionalized Carbon Dots as Template," *Ceramics International* 44 (2018): 16844–16850, https://doi.org/10.1016/j.ceramint.2018.06.120.

25. R. Xiong, X. F. Zhang, M. Krecker, S. W. Kang, M. J. Smith, and V. V. Tsukruk, "Large and Emissive Crystals From Carbon Quantum Dots Onto Interfacial Organized Templates," *Angewandte Chemie International Edition* 59 (2020): 20167–20173, https://doi.org/10.1002/anie.202008748.

26. X. G. Zhai, J. P. Gao, X. X. Wang, et al., "Inverse Pickering Emulsions Stabilized by Carbon Quantum Dots: Influencing Factors and Their Application as Templates," *Chemical Engineering Journal* 345 (2018): 209–220, https://doi.org/10.1016/j.cej.2018.03.075.

27. J. S. Wei, C. Ding, P. Zhang, et al., "Robust Negative Electrode Materials Derived From Carbon Dots and Porous Hydrogels for High-Performance Hybrid Supercapacitors," *Advanced Materials* 31 (2019): 1806197, https://doi.org/10.1002/adma.201806197.

28. J. S. Wei, T. B. Song, P. Zhang, X. Q. Niu, X. B. Chen, and H. M. Xiong, "A New Generation of Energy Storage Electrode Materials Constructed From Carbon Dots," *Materials Chemistry Frontiers* 4 (2020): 729–749, https://doi.org/10.1039/C9QM00554D.

16136829, 0, Downloaded from https://onlinelibrary.wiley.com/doi/10.1002/smll.76319 by Huan-Ming Xiong - Fudan University , Wiley Online Library on [19/10/2026]. See the Terms and Conditions (https://onlinelibrary.wiley.com/terms-and-conditions) on Wiley Online Library for rules of use; OA articles are governed by the applicable Creative Commons License

29. P. Zhang, D. Bin, J. S. Wei, et al., "Efficient Oxygen Electrocatalyst for Zn–Air Batteries: Carbon Dots and Co_9 S_8 Nanoparticles in a N,S-Codoped Carbon Matrix," *ACS Applied Materials & Interfaces* 11 (2019): 14085–14094, https://doi.org/10.1021/acsami.8b22557.

30. Y. J. Huang, X. Zhong, X. Y. Hu, et al., "Rationally Designing Closed Pore Structure by Carbon Dots to Evoke Sodium Storage Sites of Hard Carbon in Low-Potential Region," *Advanced Functional Materials* 34 (2024): 2308392, https://doi.org/10.1002/adfm.202308392.

31. Y. H. Gao, H. X. Huo, Y. M. Chen, et al., "2D WS_2 Based Asymmetric Schottky Photodetector With High Performance," *Advanced Functional Materials* 7 (2025): 24953.

32. J. Huang, C. Liu, Y. Z. Jin, and J. C. Chen, "Hierarchical Porous Carbon Synthesis by Carbonized Polymer Dots-Based Sacrificial Template for High-Performance Supercapacitors," *Chemical Engineering Journal* 461 (2023): 141930, https://doi.org/10.1016/j.cej.2023.141930.

33. H. W. Sun, X. R. Zhang, B. J. Wang, T. L. He, and H. M. Xiong, "Porous Materials Fabricated Using Carbon Dots," *Materials Chemistry Frontiers* 9 (2025): 3381–3396, https://doi.org/10.1039/D5QM00563A.

34. X. R. Zhang, T. B. Song, T. L. He, et al., "Sub-Nanometer Porous Carbon Materials for High-Performance Supercapacitors Using Carbon Dots as Self-templated Pore-Makers," *Advanced Functional Materials* 35 (2025): 2419219, https://doi.org/10.1002/adfm.202419219.

35. C. Young, J. J. Lin, J. Wang, et al., "Significant Effect of Pore Sizes on Energy Storage in Nanoporous Carbon Supercapacitors," *Chemistry—A European Journal* 24 (2018): 6127–6132, https://doi.org/10.1002/chem.201705465.

36. J. Yang, H. L. Wu, M. Zhu, et al., "Optimized Mesopores Enabling Enhanced Rate Performance in Novel Ultrahigh Surface Area Meso-/Microporous Carbon for Supercapacitors," *Nano Energy* 33 (2017): 453–461, https://doi.org/10.1016/j.nanoen.2017.02.007.

37. Y. L. Xu, C. Wang, H. Zhuo, D. R. Zhou, and Q. J. Song, "The Function-Oriented Precursor Selection for the Preparation of Carbon Dots," *Nano Research* 16 (2023): 11221–11249, https://doi.org/10.1007/s12274-023-5873-x.

38. D. W. Boukhvalov, V. Y. Osipov, D. Murzalinov, A. Serikkanov, and H. Bi, "A Comprehensive Model of Carbon Nanodots With 0.21 nm Lattice Fringes Patterns," *Carbon* 225 (2024): 119101, https://doi.org/10.1016/j.carbon.2024.119101.

39. H. Ding, S. B. Yu, J. S. Wei, and H. M. Xiong, "Full-Color Light-Emitting Carbon Dots With a Surface-State-Controlled Luminescence Mechanism," *ACS Nano* 10 (2016): 484–491, https://doi.org/10.1021/acsnano.5b05406.

40. Y. Yuan, Z. W. Chen, H. X. Yu, et al., "Heteroatom-Doped Carbon-Based Materials for Lithium and Sodium Ion Batteries," *Energy Storage Materials* 32 (2020): 65–90, https://doi.org/10.1016/j.ensm.2020.07.027.

41. S. J. Mohammed, K. M. Omer, and F. E. Hawaiz, "Deep Insights to Explain the Mechanism of Carbon Dot Formation at Various Reaction Times Using the Hydrothermal Technique: FT-IR, ^{13}C-NMR, ^{1}H-NMR, and UV-Visible Spectroscopic Approaches," *RSC Adv* 13 (2023): 14340.

42. W. C. Wu, H. Y. T. Chen, S. C. Lin, et al., "Nitrogen-Doped Carbon Nanodots Prepared From Polyethylenimine for Fluorometric Determination of Salivary Uric Acid," *Microchimica Acta* 186 (2019): 166, https://doi.org/10.1007/s00604-019-3277-0.

43. Y. B. Song, S. J. Zhu, S. T. Zhang, et al., "Investigation From Chemical Structure to Photoluminescent Mechanism: A Type of Carbon Dots From the Pyrolysis of Citric Acid and An Amine," *Journal of Materials Chemistry C* 3 (2015): 5976–5984, https://doi.org/10.1039/C5TC00813A.

44. J. P. Zobel, M. Heindl, J. J. Nogueira, and L. González, "Vibrational Sampling and Solvent Effects on the Electronic Structure of the Absorption Spectrum of 2-Nitronaphthalene," *Journal of Chemical Theory and Computation* 14 (2018): 3205–3217, https://doi.org/10.1021/acs.jctc.8b00198.

45. Y. Yu, Y. Z. Zhao, Y. S. Mi, et al., "Exploration of Optical Properties of Novel Pyrene Derivatives Modified by Click Functionalization," *Crystals* 12 (2022): 1295, https://doi.org/10.3390/cryst12091295.

46. Z. Y. Li, X. Y. Gao, L. Wu, K. W. Wang, and N. Kobayashi, "Preparation of Activated Carbons From Poplar Wood by Chemical Activation With KOH," *Journal of Porous Materials* 24 (2017): 193–202, https://doi.org/10.1007/s10934-016-0252-6.

47. X. Wang, Z. H. Qin, X. Q. Yang, Q. Chen, and Z. Lin, "Synthesis of Tremella-Like porous carbon With Oxygen-Containing Functional Groups for High-Performance Supercapacitor," *Diamond and Related Materials* 108 (2020): 107995, https://doi.org/10.1016/j.diamond.2020.107995.

48. T. Wang, J. Guo, Y. Guo, J. Feng, and D. L. Wu, "Nitrogen-Doped Carbon Derived From Deep Eutectic Solvent as a High-Performance Supercapacitor," *ACS Applied Energy Materials* 4 (2021): 2190–2200, https://doi.org/10.1021/acsaem.0c02703.

49. P. X. Ren, D. L. Wu, Y. F. Zheng, T. Wang, and D. Z. Jia, "Unlocking Fast Lithium Ion Migration in Zirconium-Based Fluoride Solid Electrolytes," *Advanced Functional Materials* 37 (2025): 08314, https://doi.org/10.1002/adfm.202527571.

50. F. Xu, Y. X. Zhai, E. Zhang, et al., "Ultrastable Surface-Dominated Pseudocapacitive Potassium Storage Enabled by Edge-Enriched N-Doped Porous Carbon Nanosheets," *Angewandte Chemie International Edition* 59 (2020): 19460–19467, https://doi.org/10.1002/anie.202005118.

51. X. Li, M. X. Sun, C. Y. Xu, et al., "Fast Kinetic Carbon Anode Inherited and Developed From Architectural Designed Porous Aromatic Framework for Flexible Lithium Ion Micro Capacitors," *Advanced Functional Materials* 33 (2023): 2300460, https://doi.org/10.1002/adfm.202300460.

52. D. Hulicova-Jurcakova, M. Seredych, G. Q. Lu, and T. J. Bandosz, "Combined Effect of Nitrogen- and Oxygen-Containing Functional Groups of Microporous Activated Carbon on its Electrochemical Performance in Supercapacitors," *Advanced Functional Materials* 19 (2009): 438–447, https://doi.org/10.1002/adfm.200801236.

53. J. Du, Y. Zhang, H. J. Lv, and A. B. Chen, "Silicate-Assisted Activation of Biomass Towards N-Doped Porous Carbon Sheets for supercapacitors," *Journal of Alloys and Compounds* 853 (2021): 157091, https://doi.org/10.1016/j.jallcom.2020.157091.

54. L. Yang, T. Wang, and D. L. Wu, "Porous Nitrogen-doped Reduced Graphene Oxide Gels as Efficient Supercapacitor Electrodes and Oxygen Reduction Reaction Electrocatalysts," *Chinese Journal of Chemistry* 38 (2020): 1123–1131, https://doi.org/10.1002/cjoc.201900482.

55. R. Zhang, X. X. Jing, Y. T. Chu, et al., "Nitrogen/Oxygen Co-Doped Monolithic Carbon Electrodes Derived From Melamine Foam for High-Performance Supercapacitors," *Journal of Materials Chemistry A* 6 (2018): 17730–17739, https://doi.org/10.1039/C8TA06471G.

56. Y. C. Liu, M. J. Shi, M. N. Han, et al., "Spontaneous Exfoliation and Tailoring Derived Oxygen-Riched Porous Carbon Nanosheets for Superior Li^+ Storage Performance," *Chemical Engineering Journal* 387 (2020): 124104, https://doi.org/10.1016/j.cej.2020.124104.

57. Y. Li, L. Liu, Y. Wu, et al., "Facile Synthesis of Nitrogen-Doped Carbon Materials With Hierarchical Porous Structures for High-Performance Supercapacitors in Both Acidic and Alkaline Electrolytes," *Journal of Materials Chemistry A* 7 (2019): 13154–13163, https://doi.org/10.1039/C9TA00890J.

58. Z. X. Guo, Z. W. Tian, G. G. Duan, et al., "Cellulose Intercalation Activation of Natural Ramie Fiber Derived Carbon Electrode for Flexible Supercapacitors," *Chemical Engineering Journal* 501 (2024): 157702, https://doi.org/10.1016/j.cej.2024.157702.

59. J. C. Zhang, J. W. Luo, Z. X. Guo, et al., "Ultrafast Manufacturing of Ultrafine Structure to Achieve An Energy Density of Over 120 Wh kg^{-1} in Supercapacitors," *Advanced Energy Materials* 13 (2023): 2203061, https://doi.org/10.1002/aenm.202203061.

16136829, 0, Downloaded from https://onlinelibrary.wiley.com/doi/10.1002/smll.76319 by Huan-Ming Xiong - Fudan University , Wiley Online Library on [19/10/2026]. See the Terms and Conditions (https://onlinelibrary.wiley.com/terms-and-conditions) on Wiley Online Library for rules of use; OA articles are governed by the applicable Creative Commons License

60. L. Yao, J. S. Lin, Y. Y. Chen, et al., "Graphene/MXene Fibers-Enveloped Sulfur Cathodes for High-Performance Li-S Batteries," *InfoMat* 4 (2022): 12278.

61. Y. Lin, C. Huang, C. X. Huang, et al., "Cellulose Regulated Lignin/Cellulose-Based Carbon Materials With Hierarchical Porous Structure for Energy Storage," *Advanced Composites and Hybrid Materials* 7 (2024): 51, https://doi.org/10.1007/s42114-024-00850-5.

62. F. T. Ran, X. B. Yang, X. Q. Xu, S. W. Li, Y. Y. Liu, and L. Shao, "Green Activation of Sustainable Resources to Synthesize Nitrogen-Doped Oxygen-Riched Porous Carbon Nanosheets Towards High-Performance Supercapacitor," *Chemical Engineering Journal* 412 (2021): 128673, https://doi.org/10.1016/j.cej.2021.128673.

63. D. Zhang, J. H. Kim, W. T. Hong, et al., "Advanced Soft Materials, Sensor Integrations, and Applications of Wearable Flexible Hybrid Electronics in Healthcare, Energy, and Environment," *Advanced Energy Materials* 32 (2026): 1901924, https://doi.org/10.1002/aenm.70900.

64. B. Peng, Y. W. Zhu, S. Chu, and H. Y. Zhang, "N-Doped Hierarchical Porous Carbons Derived From Heavy Bio-Oil for Supercapacitor Applications," *Chemical Engineering Journal* 507 (2025): 160551, https://doi.org/10.1016/j.cej.2025.160551.

65. Y. Chen, X. H. Liu, X. T. Ma, et al., "Biomass-Based 2D Porous Carbon With Cross-Linked Nanosheets via Co-Hydrothermal Pretreatment for High-Performance Supercapacitors," *Chemical Engineering Journal* 519 (2025): 165145, https://doi.org/10.1016/j.cej.2025.165145.

Supporting Information

Additional supporting information can be found online in the Supporting Information section.

Supporting File: smll76319-sup-0001-SuppMat.docx.

16136829, 0, Downloaded from https://onlinelibrary.wiley.com/doi/10.1002/smll.76319 by Huan-Ming Xiong - Fudan University , Wiley Online Library on [19/10/2026]. See the Terms and Conditions (https://onlinelibrary.wiley.com/terms-and-conditions) on Wiley Online Library for rules of use; OA articles are governed by the applicable Creative Commons License